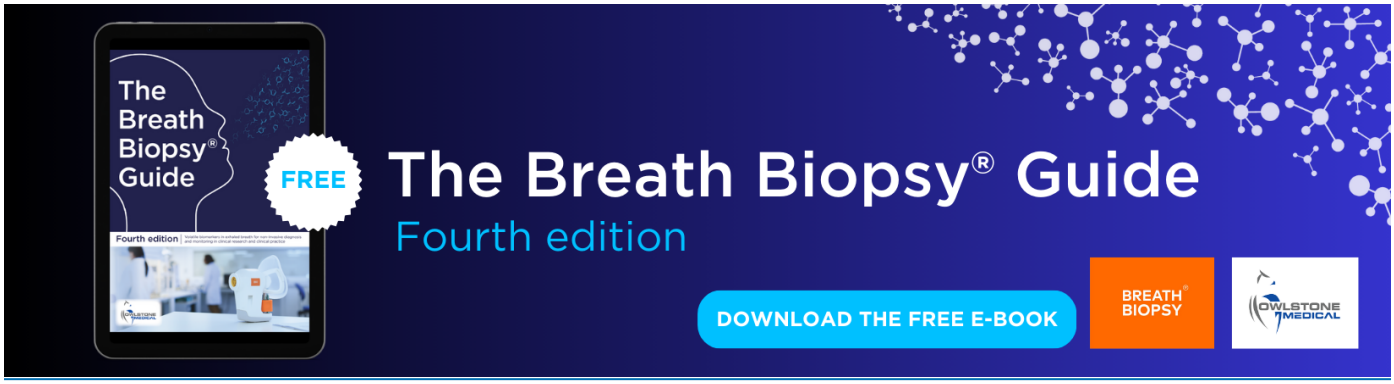
INCLUSIVE PUBLISHING
TRUSTED SCIENCE

Impact of sulfur content on thermo-capillarity and melt pool dynamics in laser powder bed fusion of 316L powders

To cite this article: Zhiyong Li *et al* 2023 *Mater. Res. Express* **10** 126502



Materials Research Express

PAPER

Impact of sulfur content on thermo-capillarity and melt pool dynamics in laser powder bed fusion of 316L powders

Zhiyong Li[1,*], **Xinfeng Kan**[2] and **Yanjun Yin**[3]

[1] Welding and Additive Manufacturing Centre, Cranfield University, Cranfield, Bedfordshire, MK43 0AL, United Kingdom
[2] Jiangsu University of Science and Technology, Zhenjiang 212100, Jiangsu, People's Republic of China
[3] Changzhou Institute of Technology, Changzhou 213032, Jiangsu, People's Republic of China
[*] Author to whom any correspondence should be addressed.

E-mail: zhiyong.li@cranfield.ac.uk

Keywords: melt pool dynamics, thermo-capillary, fluid dynamics, laser powder bed fusion, 316L powders, surface-active element

OPEN ACCESS

RECEIVED
9 June 2023

REVISED
19 October 2023

ACCEPTED FOR PUBLICATION
17 November 2023

PUBLISHED
5 December 2023

Original content from this work may be used under the terms of the Creative Commons Attribution 4.0 licence.

Any further distribution of this work must maintain attribution to the author(s) and the title of the work, journal citation and DOI.

Abstract

A three-dimensional numerical model is developed to investigate the influence of sulfur content on the transitions of thermo-capillarity and flow dynamics during laser powder bed fusion (LPBF) of 316L powders. The impacts of variations in sulfur contents on thermal behaviors involving heat transfer and solidification characteristics, thermo-capillarity transition, as well as the spatial and directional transitions in flow dynamics, are analyzed through mechanistic modeling techniques. It is observed that transient thermal behaviors, including melt pool profile, track morphology, and solidification processes, are significantly influenced by the contained sulfur concentration. High sulfur concentrations tend to result in finer microstructures and equiaxed grains. Through simulations, it is noted that the transition in the sign of temperature coefficient of surface tension (TCST) is more easily observable in low-sulfur level but disappears as the sulfur concentration is extremely low (0.0001%) With sulfur content increasing, a more homogenized velocity distribution is observed, accompanied with heightened flow complexity denoted by the emergence of additional branch flows and vortices. These findings offer valuable insights into the underlying physics of melt pool dynamics in the LPBF process and present a potential approach for process optimization.

1. Introduction

Laser powder bed fusion (LPBF), also known as selective laser melting (SLM), offers advantages over complex geometry, cost and time reduction, and manufacturing performance [1–4]. It has drawn numerous interests from industry communities such as aerospace, automobile, and shipbuilding, etc. However, LPBF parts are also prone to be laden with process-induced defects and limited to widespread application. Arising from the printing process, defects can be classified as lack of fusion, gas-induced pores/voids, hot cracking and discontinuity [5–9], etc. Among many underlying causes, it is identified that unexpected melt pool dynamics is one of the major contributors to process resulted defects [10, 11]. For example, keyhole dynamics and nonhomogeneous mixing are not expected in LPBF. The laser-induced keyhole inside the melt pool is considered one of the key factors that result in the porosity in the final solidified melt pool for LPBF. The non-uniform dilution of alloy elements contributes to the formation of intermetallic compounds, which may induce the cracking of solidified parts.

The melt pool dynamics in LPBF are characterized by strong coupling between multiple scales and multiple physics, involving extreme physical phenomena such as rapid solidification (μs), ultra-high cooling rate (over 10^5 K/s), and high-temperature (over 3000 K) flow dynamics. High-resolution imaging devices and tools have been incorporated into experimental research on melt pool dynamics in metal additive manufacturing to obtain reliable online observations and perform quantitative analysis of the physical details of the morphology evolution, velocity field, powder spattering, etc [12–15]. High-speed high-energy x-ray imaging in Argonne National Lab (ANL) [12], fast camera with high spatial and temporal resolution [13], optical pyrometer [14], and

© 2023 The Author(s). Published by IOP Publishing Ltd

infrared thermography [15] have been well developed and demonstrated as efficient and strong imaging technologies to capture the extreme physics. Despite obtaining insightful knowledge from reliable observation through various advanced *in situ* imaging technologies, these methods are still limited in their ability to provide sufficient details on the melt pool dynamics due to the restrictions arising from imaging mechanisms based on optical and thermal theories and device capability. Furthermore, most of the groups interested in metal AM can hardly afford such cost-consuming research.

The rapid advancement of Computational Fluid Dynamics (CFD) technology and computer engineering has significantly facilitated the adoption of modeling and simulation approaches. These tools provide physics-informed descriptions, thereby supporting the derivation of relationships between process, structure, and material properties in metal additive manufacturing [16, 17]. To gain insights into the laser-material interaction, heat transfer, phase change, powder behavior, flow dynamics, and the evolution of melted track morphology, as well as the solidification phenomenon within LPBF, extensive computational modeling works at the mesoscale, involving methods like the Finite Element Method (FEM) [18], Finite Volume Method (FVM) [19–21], and Discrete Element Method (DEM) [22, 23], have been undertaken. Insights obtained from peer-reviewed publications have fundamentally elucidated the impacts of processing parameters through parametric studies and dimensional analyses [24]. They have also contributed to revealing the formation mechanisms of underlying process-induced defects such as lack of fusion, porosity, and discontinuity. Furthermore, these studies have provided characterizations of the evolving morphology within the melt pool (including features such as the fusion line and gas/liquid interface) and the surface roughness of multi-track, multi-layer as-built components.

Materials used in metal additive manufacturing can be categorized into two groups based on their sulfur content: high-sulfur powders like 316L and Inconel 718, and low-sulfur powders including Ti6Al4V and AlSi10Mg. The increment of sulfur content can lead to significant transitions in melt pool dynamics. Particularly, the presence of sulfur in high-sulfur powders can induce a transition in the temperature coefficient of surface tension (TCST) under specific conditions [25]. Furthermore, it can impact the thermo-capillary force, which serves as the primary driving force governing melt pool dynamics [26]. Consequently, both the direction and magnitude of the melt pool's flow pattern can be substantially altered. The transition of TCST induced by sulfur and resulting changes in flow patterns have garnered significant attention in various laser manufacturing techniques of high-sulfur materials, such as laser welding of stainless steel [27], laser polishing of stainless steel [28], and laser direct energy deposition of Co-based powders [29]. Particularly, great efforts have been denoted to explore the impact of surface-active elements involving sulfur, selenium, etc, on the melt pool dynamics by the welding community [30–36], both numerically and experimentally. Heiple *et al* [30] demonstrated that the addition of selenium to the molten pool increases the depth/width ratio for conduction mode welding but has little influence on melt pool dimensions for keyhole welding. This conclusion acts for gas tungsten arc (GTA), laser, and electron beam welds. Pitscheneder *et al* [31] concluded that the concentration of sulfur affects both the temporal evolution and the final shape of the melt pool only when the convective heat transfer is important, i.e., at high Peclet numbers. Moreover, numerical modeling further reveals the mechanism of sulfur-induced transitions of the sign of TSCT and the flow pattern inside the weld pool [32, 33]. Furthermore, the impact of sulfur-effect on flow instability and melt pool oscillation in GTA has been thoroughly studied by Ebrahimi *et al* [34–36]. They found that the sulfur-effect on Marangoni convection enhances the flow instabilities for the internal flow and the reduction of sulfur content induces a contrary outward flow from the view of the melt pool surface, subsequently leading to a wide and shallow melt pool. These technologies share similar physics with LPBF.

The sulfur-induced transition of thermo-capillarity (TCST) and the resulting changes in melt pool dynamics have also drawn the attention of researchers who have interests in LPBF. A 3D thermal-fluid model was developed by Le *et al* [37] to reveal the effect of sulfur level on melt pool dynamics in LPBF. It is demonstrated that for stainless steel powders with a higher sulfur content, an inward Marangoni flow is prompted, which can increase the melt pool depth and reduce the porosity of the as-built part. In-situ direct observation of the melt pool dynamics for metal additive manufacturing was carried out by Aucott *et al* [38] through the high-energy synchrotron experiment, in which the transitions of flow dynamics are directly observed when the sign of temperature coefficient of surface tension is changed. Mathematical descriptions of TCST incorporated in proposed numerical models are expressed as a function of local sulfur content and temperature at the gas/liquid interface of the melt pool with references from [27–29, 31–37]. In these references, TCST is a variable and its transition from negative to positive or the inverse transition is considered. In contrast, it is simplified as a negative constant in references [16–23], where no consideration is given to sign transitions.

In a word, the utilization of a constant assumption is a dependable approach when low-sulfur powders are employed. However, this approach is not justifiable when simulating the melt pool dynamics for high-sulfur powders, such as 316L. In this situation, it is advisable to incorporate a functional description of the TCST. After conducting a thorough review of the existing literature [1–38], it can be inferred that the sulfur-induced transition of TCST and its consequent impact on flow pattern during LPBF of high-sulfur powders still have not

been elucidated through high-fidelity, powder-scale multi-physics modeling. The lack of physical details about the powder-scale melt pool dynamics variations induced by sulfur-effect restricts the process adjustment aimed at microstructure refinement and property improvement for the real LPBF process.

To address this research gap, an enhanced powder-scale transient model that incorporates a surface tension sub-model is developed. The primary objective of this model is to explore the fundamental physical mechanisms underlying the sulfur-induced transition of thermo-capillarity and the resulting shifts in flow patterns during the LPBF of 316L powders. Considering the permissible maximum sulfur content in 316L and its globally recognized equivalent alloys, the current model is initially configured to investigate melt pool morphology and dimension through a systematic parametric examination of sulfur concentration. Subsequently, the numerical analysis to elucidate the sulfur-induced transition of TCST and its consequential impact on flow dynamics is performed. This work continuously explores the influence of sulfur concentration on the spatial and directional characteristics of melt pool dynamics. To this end, the mechanism that comprehensively describes the effects of sulfur on thermo-capillarity and flow dynamics across varying sulfur concentrations is proposed. The aim is to identify potential strategies for mitigating process-induced defects and enhancing the quality of as-built 316L components manufactured through LPBF.

2. Numerical procedure

2.1. Geometry and discretization

The size of 316L powders changes from 20 μm to 50 μm. A powder layer with a thickness of 50 μm is randomly generated and filled into the powder bed with the dimension of 1000 μm $\times$ 400 μm $\times$ 150 μm. The model geometry is uniformly discretized by tetrahedral cells with the size of 5 $\times$ 10^{-6}m with the mesh-sensitivity test in advance.

2.2. Powder-scale CFD model

An improved 3D transient powder-scale melt pool dynamics model incorporated with a surface tension sub-model is proposed based on the software platform of FLOW-3D to simulate the sulfur-effect on thermo-capillarity in LPBF of 316L powders. SIMPLE solver based on FVM is utilized for iteration with the maximum time step of $10^{-12}s$. The mathematical relation describing surface tension/TCST, local temperature, and sulfur content is obtained from [25]. Volume of Fluid method (VOF) [39] is incorporated to construct the melt pool profile and track morphology, which can be expressed by:

$$\frac{\partial F}{\partial t} + \nabla \cdot (F\boldsymbol{u}) = 0 \tag{1}$$

As described in equation (1), phase fraction F is calculated in each cell, while fluid velocity $\boldsymbol{u}$ is obtained from the solution of the momentum equation. Thus, the free surface of melt pool and melt track can be reconstructed in each iteration.

2.3. Thermo-physical properties

316L powders have garnered great attention in LPBF due to its strength, antioxidation properties, and corrosion resistance. The allowable content of suflur in 316L varies by global standards. It is 0.03% in US ASTM AISI and SAE, EU EN, and France ANFOR, while limited to 0.015% by China GB and England BS. Thermophysical properties of 316L powders and numerical constants for the current modelling are listed in table 1.

2.4. Boundary conditions

High-fidelity modelling depends on the accurate boundary conditions, and the detailed descriptions of energy aboundary and momentum bounday are given by followings.

2.4.1. Energy boundary

The energy boundary at gas/liquid surface of melt pool is given as:

$$-K\frac{\partial T}{\partial z} = (1 - R_\lambda)\cos\theta\frac{2P}{\pi {r_b}^2}\exp\left(-\frac{2r^2}{r_b^2}\right) - h_c(T - T_{ref}) - \sigma_b\varepsilon(T^4 - T_{ref}^4) \tag{2}$$

In equation (2), the first term at right hand denotes laser heat input, in which θ is the laser incident angle relative to the gas/liquid interface, and r represents the distance to laser center. The reflectivity and the resultant absorption of laser energy are both assumed constant at the current work. The absorption is a variable and depend on laser characteristics, laser-ray incident angle, surface temperature, and base-material composition [42, 43]. The functional description is more realistic and can enhance the modelling accuracy. Based on the

Table 1. Thermophysical properties of 316L powders and numerical constants for the current modelling of LPBF [17, 29, 40, 41].

Properties and constants				
Property	Symbol	Unit	Value	Reference
Density in solid	ρ	kg/m^3	$8084 + 0.4209 \times T - 3.9 \times 10^{-5} \times T^2$	[17]
Density in liquid		kg/m^3	$7433 + 0.0393 \times - 1.8 \times 10^{-4} \times T^2$	[17]
Thermal conductivity in solid		W/m/K	$12.41 + 0.003279 \times T$	[17]
Thermal conductivity in liquid		W/m/K	$9.248 + 0.01571 \times T$	[17]
Specific heat in solid	C_p	J/kg/K	755	[17]
Specific heat in liquid	C_p	J/kg/K	$462 + 0.134 \times T$	[17]
Solidus temperature	T_s	K	1788	[40]
Liquidus temperature	T_l	K	1808	[40]
Temperature coefficient of surface tension		N/m/K	-4.3×10^{-4}	[41]
Surface tension		N/m	1.7	[41]
Enthalpy of fusion	L_m	kJ/kg	247	[41]
Dynamic viscosity		Pa·s	6.0×10^{-3}	[41]
Numerical constants				
Constant	Symbol	Unit	Value	Reference
Reflectivity	R_λ	1	0.7	—
Ambient temperature	T_{ref}	K	300	—
Heat transfer coefficient of convection	h_c	W/m^2/K	100	[29]
Stefan-Boltzmann constant	σ_b	W/m^2/K	5.67×10^{-8}	—
Emissivity		1	0.2	—
Processing parameters	Symbol	Unit	Value	Reference
Laser power				—
Laser radius	r_b		50	—
Scanning speed	V			—
Powder layer thickness	h			—

conclusion from Amin *et al* [43], the laser energy absorbed by melt pool is underestimated in the current modelling as the reflectivity is 0.7 and the resultant absorption is constant 0.3. As a result, the calculated peak temperature and melt pool dimensions are expected to be smaller than the real situation.

Moreover, the second term and third term denote the heat loss caused by heat convection and radiation, respectively. Heat transfer coefficient h_c is strengthened by the shielding gas flow and determined with the reference from publications [29]. The emissivity ε at the current study comes from modelling experience for LPBF. Only the second and the third terms are included in the energy boundary for the other faces.

2.4.2. Momentum boundary

Momentum condition at gas/liquid surface of melt pool can be expressed as:

$$\left[-p\boldsymbol{I} + \mu(\nabla \boldsymbol{u} + (\nabla \boldsymbol{u})^T) - \frac{2}{3}\boldsymbol{u}(\nabla \cdot \boldsymbol{u})\boldsymbol{I}\right] \cdot \boldsymbol{n} = \sigma\kappa\boldsymbol{n} + \gamma\nabla_s \quad T \tag{3}$$

The first and second term at right hand represent capillary force and thermal capillary force, respectively. $p$is the pressure. κ is the gas/liquid surface curvature. The momentum boundary for the other boundaries of the model is no slip.

2.5. Assumptions

The current modeling is performed under some key assumptions. Flow dynamics are assumed to be Newtonian, laminar, and incompressible with the Boussinesq approximation. Particularly, fluid flow in the mushy zone is described by a porous flow based on the Carmen-Kozeny relation [44]. Evaporation-induced heat loss and mass loss are not included because the LPBF process is in conduction mode under the current processing parameters. The thermal properties of 316L powders are considered a function of temperature but are sulfur independent.

2.6. Sub-model of surface tension

The mathematical relation of surface tension/TCST, local temperature, and sulfur content is derived from Sahoo *et al* [25].

$$\sigma(T) = \sigma - \gamma(T - T_l) - R_u T\Gamma_s \ln(1 + K\alpha_s) \tag{4}$$

$$\frac{\partial\sigma}{\partial T} = -\gamma - R_u\Gamma_s \ln(1 + K\alpha_s) - \frac{K\alpha_s}{1 + K\alpha_s} \tag{5}$$

$$K = k_l \exp\left(-\Delta H^0 / R_u T\right) \tag{6}$$

In relations, R_u is universal gas constant, Γ_s is the surface excess at saturation, k_l is the constant of segregation entropy, and ΔH_0 is the standard heat of absorption. Referencing the published literatures [25–29], Γ_s is 1.3×10^{-5}Kmol/m^2, k_l is 3.18×10^{-3}, and ΔH^0 is -1.88×10^5KJ/kmol in the current modeling. α_s denotes the sulfur activity and is represented by the percentage of sulfur content. Consequently, both the surface tension and TCST are the function of local temperature and sulfur content. Different from the constant TCST with negative value when sulfur-effect is not considered, the TCST changes in every time step and the sign transition may occur in certain situations, e.g., the transition from positive to negative value or the inverse transition. In sulfur-free situation, the last term at right hand of equation (4) is not considered and the last two terms of equation (5) disappear, which results in the constant TCST with negative value.

2.7. Governing equations

Heat transfer, phase change, powder fusion, as well as fluid flow are all simulated in the proposed transient powder-scale model. The mass, momentum, and energy conservation of equations are all incorporated to describe melt pool dynamics, which could be respectively expressed as follows:

$$\nabla \cdot (\rho \mathbf{u}) = 0 \tag{7}$$

$$\rho \frac{\partial \boldsymbol{u}}{\partial t} + \rho(\mathbf{u} \cdot \nabla)\boldsymbol{u} = \nabla \cdot (\mu \nabla \boldsymbol{u}) - \nabla \boldsymbol{p} + \rho \boldsymbol{g}$$

$$-A_{mush}\boldsymbol{u}(1 - f_l)^2/(f_l^3 + M) \tag{8}$$

$$\rho C_p^{eq} \frac{\partial T}{\partial t} + \rho C_p^{eq} \boldsymbol{u} \cdot \nabla T = \nabla \cdot (\lambda \nabla T) + \rho \frac{\partial (\Delta H)}{\partial t} - \rho \boldsymbol{u} \nabla (\Delta H) \tag{9}$$

In relations, $\boldsymbol{u}$ denotes the velocity vector, and $\boldsymbol{g}$ represents the gravitational acceleration vector. μ is temperature-dependent dynamics viscosity and contributes to the construction of melt pool shape. For simplification, it is 100 Pa · s when the temperature is below liquidus and 6×10^{-3}Pa · s when temperature beyond liquidus. A_{mush} is a numerical constant and set as 10^7kg/m^3 · s. f_l represents the liquid phase fraction, which is 0 below solidus (T_s) and 1 above liquidus (T_l), and described by $f_l = \frac{T - T_s}{T_l - T_s}$ when the temperature is between solidus and liquidus. M is a numerical constant and set as 10^{-4}. A_{mush} describes the mushy zone morphology and denotes the restriction for the porous flow, which has significant influence on the solid/liquid boundary [45]. C_p^{eq} is the equivalent specific:

$$C_p^{eq} = C_p + \frac{L_m}{\sqrt{\pi \Delta T^2}} \exp\left[-\frac{(T - T_m)^2}{\Delta T^2}\right] \tag{10}$$

in which $\Delta T = (T_l - T_s)/2$ and $T_m = (T_l + T_s)/2$, representing the solidification interval and the melting temperature, respectively. In addition, $\Delta H = L_m f_l$ is the specific enthalpy caused by phase change.

3. Results and discussion

Conduction mode is preferred in real LPBF manufacturing as the porosity in final solidified part is susceptible to keyhole mode. Consequently, most of the previous modelling works for LPBF focus on conduction mode. The differences in melt pool dynamics between sulfur free situation and 0.03% sulfur situation are thoroughly discussed and compared in our previsou publication [46]. Some major conclusions are drawn from [46]. The new flow pattern of combined outward-inward flow is observed because of the sulfur-induced transition of surface tension. The maximum velocity decreases in 0.03% sulfur situation because the sulfur-induced complex flow lowers the spatial gradient of temperature and decreases the driving force. Melt pool dynamics in 0.03% sulfur situation are more complex with more vortexes induced at transverse section and more branch flows and mixing positions of branch flow (MPBF) observed at longitudinal section. More detailed comparisons and discussion are presented in reference [46].

For the current work, the effects of sulfur content variations on thermal behavior, thermo-capillarity, and flow dynamics are analyzed and emphasized through a systematic parametric study.

3.1. Sulfur-effect on thermal behavior

As illustrated in figure 1(a), the proposed 3D model is discretized by unstructured tetrahedral mesh with a uniform size of $5 \times 10^{-6}m$. The final mesh system contains 895442 elements. Next, the proposed model is validated by the experimentally observed melt pool geometry from published literature [8]. As shown in figure 1 (b), the simulated result shows good correspondence with the experiment observation, which means the good accuracy and fidelity of the developed numerical model.

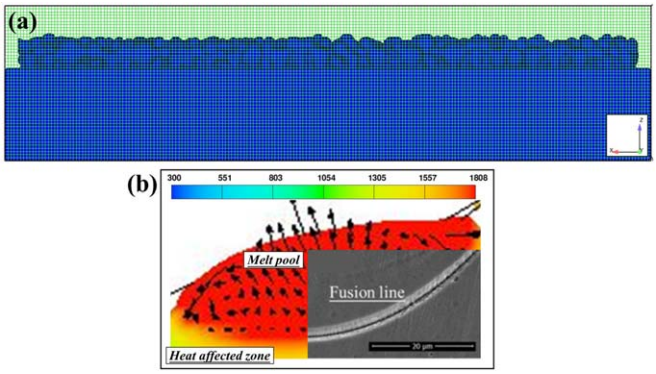


Figure 1. (a) Mesh discretization and (b) Validation of the proposed model. The experiment observation of the melt pool in sub-figure (b) reprinted from [8], Copyright (2021), with permission from Elsevier. (The reader is referred to the web version of this article for a better understanding).

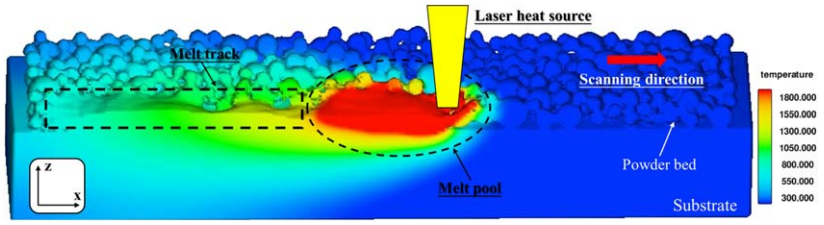


Figure 2. Temperature field, melt pool profile, and melt track morphology at the stable stage in Sul-1, corresponding to the physical time of 1100 μs. The temperature in Kelvin (K) is expressed by the color bar. (The reader is referred to the web version of this article for a better understanding).

Table 2. The distinct sulfur levels for parametric study and the corresponding occurrence of thermo-capillarity transition.

ID	Sul-1	Sul-2	Sul-3	Sul-4	Sul-5	Sul-6
Sulfur content (%)	0.0001	0.001	0.005	0.01	0.015	0.03
Thermo-capillarity transition	NA	Y	Y	Y	Y	Y

To obtain a deeper understanding of the impact of sulfur on both melt pool morphology and, notably, melt pool dynamics, a systematic parametric study regarding sulfur content is conducted, utilizing the variables outlined in table 2. The selected study cases are thoughtfully structured to encompass a broad spectrum of sulfur content scenarios, involving the released standards for 316L stainless steel and equivalent alloys worldwide. Additionally, these cases in the current study serve as valuable reference points for other materials employed in metal additive manufacturing, such as Inconel 718.

The processing parameters are listed in table 1 and remained consistent across all six situations. Figure 2 illustrates the temperature field, melt pool, and melt track morphology at the stable stage for Sul-1, in which the sulfur content is extremely low. The color contour, along with the scale bar provided on the right side, represents the transient temperature field. Regions where the local temperature exceeds the liquidus temperature of 1808K are indicated in red. Consequently, the melt pool corresponding to the current printing time is colored red and highlighted by the black dotted ellipse, with the laser heat source located at its front part. The melt track, undergoing the melting and solidification process, is marked within the black dotted rectangle. As depicted, common process-induced defects observed in LPBF, such as balling, pores/voids, and discontinuities, are absent under the current processing conditions. This suggests that the employed parameters are well-suited for achieving a defect-free melt track in the LPBF of 316L powders, even with the significantly lower sulfur content found in Sul-1. The melt pool depicted in figure 2 is in a conduction mode, wherein energy from the laser heat source is absorbed by the upper layers of powders and subsequently conducted towards the lower powders and the substrate, thereby facilitating melt pool formation and dynamic evolution.

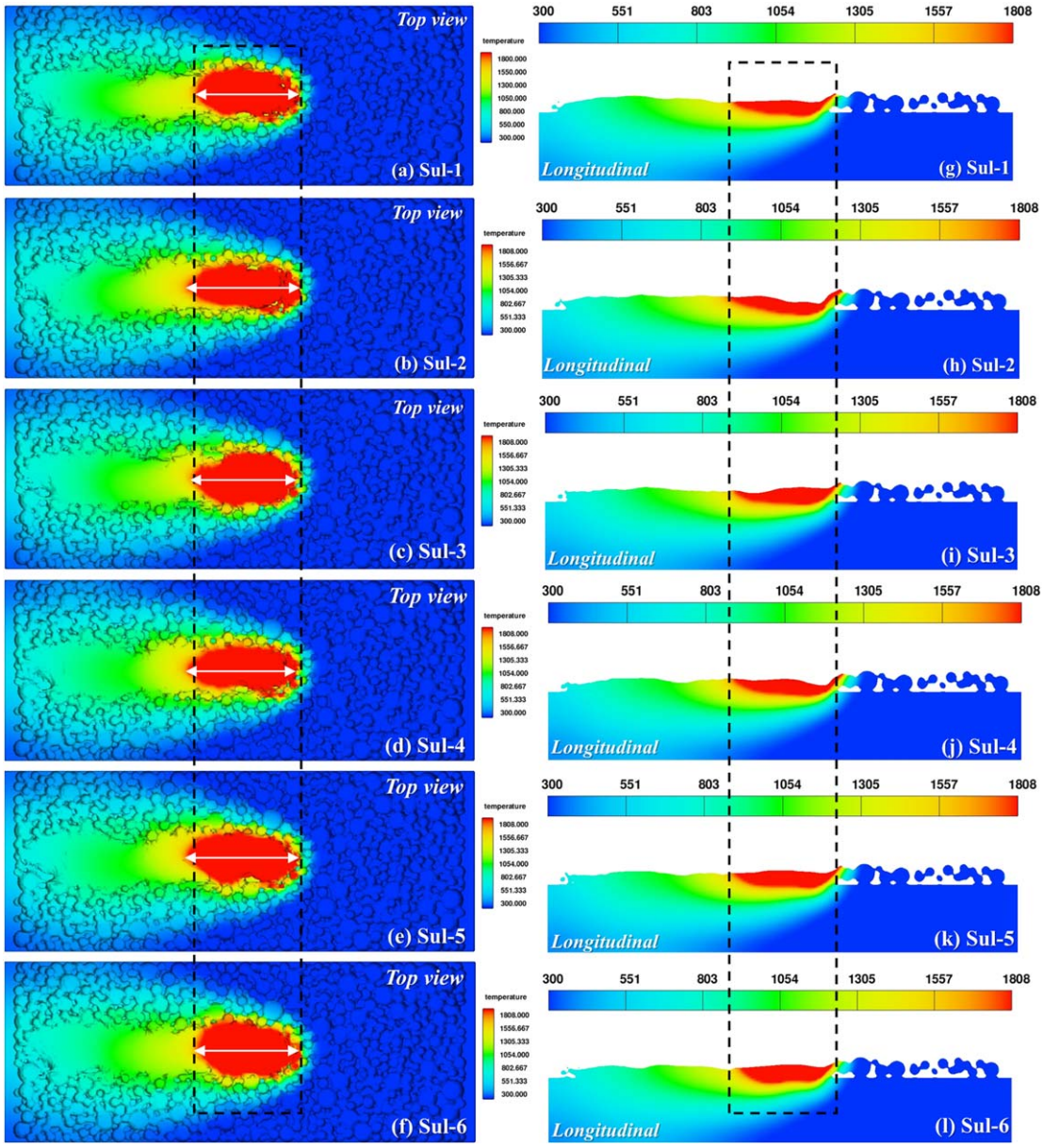


Figure 3. Temperature field, melt pool profile, and melt track morphology at the top view and longitudinal section for different cases when melt pool is stable. (a) (g) Sul-1, (b) (h) Sul-2, (c) (i) Sul-3, (d) (j) Sul-4, (e) (k) Sul-5, (f) (l) Sul-6. The temperature in Kelvin (K) is expressed by the color bar. (The reader is referred to the web version of this article for a better understanding).

Figure 3 illustrates the impact of sulfur content on the transient temperature distribution, melt pool profile, and melt track morphology for stable melt pool. The temperature field is represented by the color bar, and the melt pool profile is delineated by the black dotted rectangle. Melt pool length is indicated using white solid arrows. As the sulfur content increases, there is an initial rise followed by a subsequent decrease in melt pool length, with the maximum value occurring in the Sul-5 (0.015%). It is worth noting that melt pool duration correlates with melt pool length [47]. Consequently, solidification parameters, such as cooling rate and morphology parameters, undergo changes, potentially resulting in transitions in grain size and morphology in accordance with metallurgical theory [48]. Furthermore, as depicted in the longitudinal section, the surface roughness of the solidified track exhibits significant variation versus sulfur content, which greatly relies on the flow pattern inside the melt pool [49].

Figure 4 shows the melt pool profile and temperature field at the transverse section, as well as the 3D melt track, for all six cases. The location of the selected section is indicated by the black rectangle in the 3D sub-figure, with the scanning direction proceeding along the positive x-axis. As depicted, there is a notable variation in transverse melt pool morphology with changes in sulfur content. Subject to identical processing parameters, the peak temperature exhibits an initial increase followed by a decrease as sulfur content increases from Sul-1 to Sul-6. The melt pool depth, highlighted by black arrows and rectangle, initially drops, subsequently rise, with the

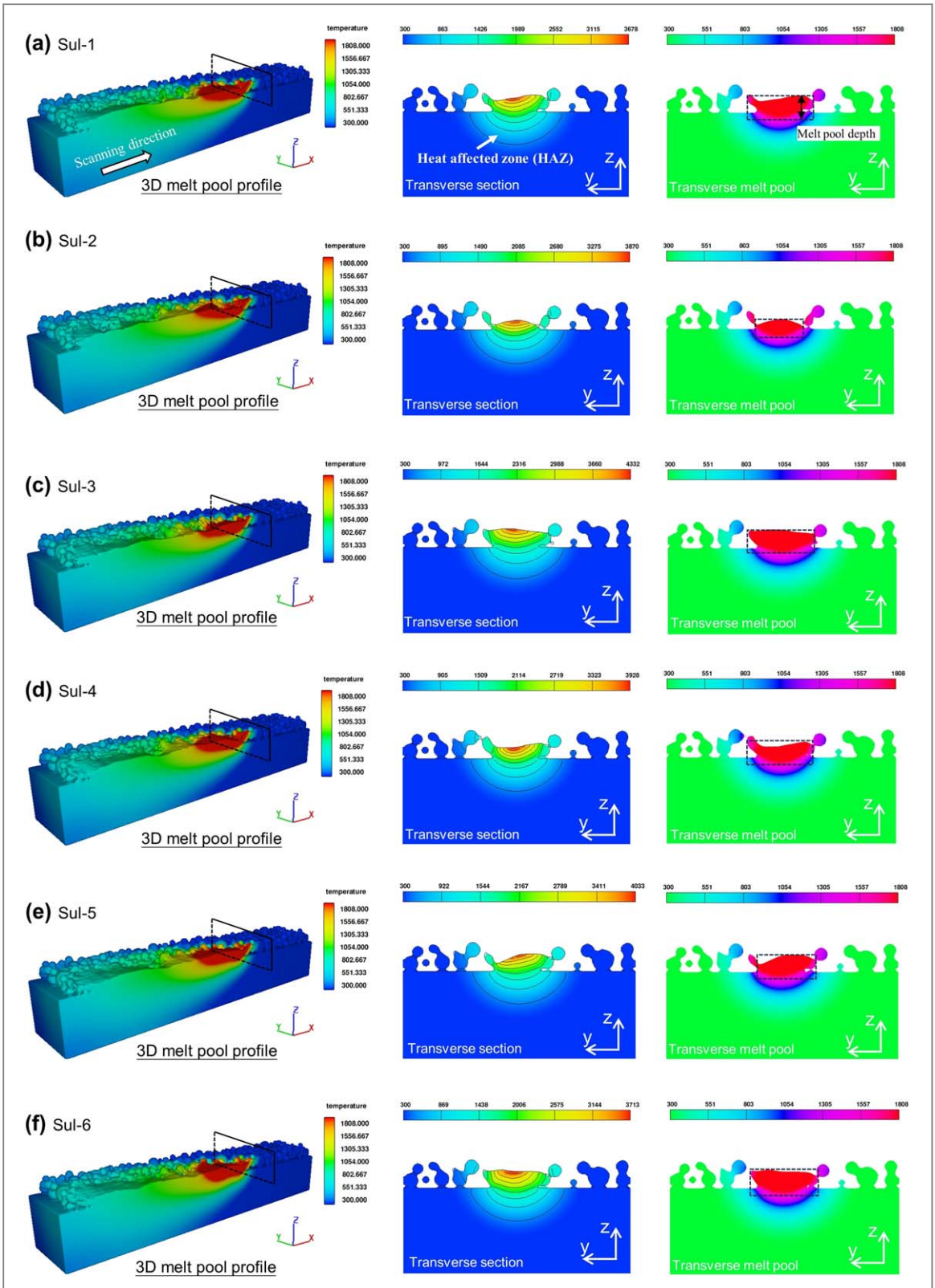


Figure 4. Temperature field with isolines, melt pool profile and melt track morphology at the transverse section for different cases when melt pool is stable. (a) Sul-1, (b) Sul-2, (c) Sul-3, (d) Sul-4, (e) Sul-5, (f) Sul-6. The temperature in Kelvin (K) is expressed by the color bar. (The reader is referred to the web version of this article for a better understanding).

sulfur content increasing. Moreover, the fluctuation of the free surface (gas/liquid interface), is considerably reduced in the situation with higher sulfur content. In summary, transient thermal behaviors, encompassing melt pool dimensions and melt track morphology, among others, are profoundly influenced by the sulfur content contained. Besides as illustrated in the transverse sections of figure 4, the heat effect zone (HAZ) presents a semi-circular shape for all the situations, which is the same as the distribution of the temperature isoline under heat conduction mode. Additionally, the distribution, and the area of HAZ change little from Sul-1 to Sul-6. It

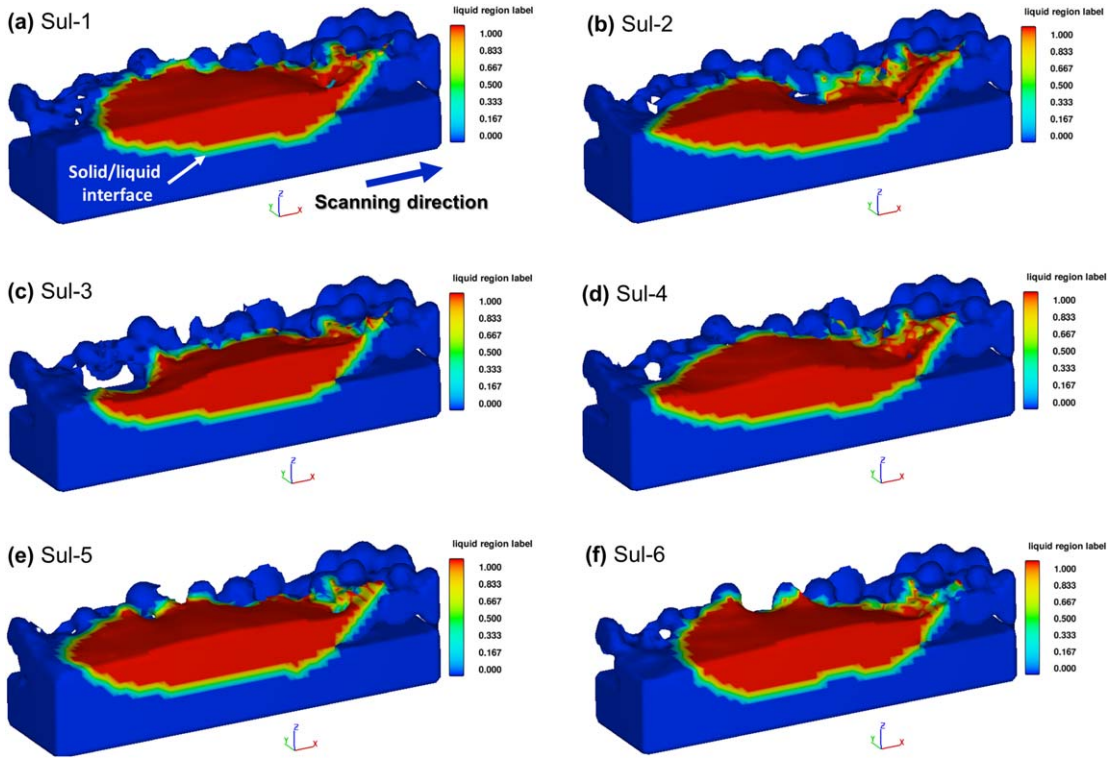


Figure 5. 3D melt pool profile with liquid region labelled for different cases. (a) Sul-1, (b) Sul-2, (c) Sul-3, (d) Sul-4, (e) Sul-5, (f) Sul-6. Color contour represents the fraction of the liquid phase. (The reader is referred to the web version of this article for a better understanding).

can be primarily concluded that the sulfur-induced transitions of heat transfer and fluid flow inside melt pool have no significant impact on the HAZ.

Figure 5 presents the 3D melt pool profile with the liquid fraction depicted by a color contour. In detail, values of one and zero represent the liquid and solid phases, respectively, while other values indicate the transition region between the two phases. To provide a clearer illustration, half of the melt pool is omitted along the *y*-axis direction, enabling a more detailed examination of the internal features within the melt pool. As sulfur content increases, the bottom of the melt pool, specifically the solid/liquid interface, undergoes significant changes. For instance, it exhibits a curved shape in Sul-1 and Sul-2 with low sulfur content but changes to a nearly flat interface in Sul-5 and Sul-6 when sulfur content is significantly elevated. What is more, this transition towards a smoother melt pool interface (solid/liquid interface) is not only observed in the longitudinal view but is also evident from three different perspectives as sulfur content increases.

Based on the transient thermal analysis of the melt pool [47], temperature gradient G and solidification rate R can be directly calculated from the developed model, subsequently the combined solidification parameters GR and G/R, in which GR is the cooling rate and G/R represents the morphology parameter. In accordance with metallurgical theory regarding the solidification process within the melt pool [48], GR determines the grain size of the solidified structure, and the grain morphology relies on the value of G/R. In specific, as GR increases, the solidified microstructure becomes finer. Planar, cellular, and equiaxed grains are prone to being observed with the drop of morphology parameter G/R. The temperature gradient, denoted as G, is perpendicular to the solidification front and can be expressed as $G=\|\nabla T\|$. On the other hand, the solidification rate, R, can be described by $R = V \bullet \cos\theta$, where V represents the heat source's movement speed, and θ signifies the angle between the scanning direction and the normal direction to the solidification front.

To make an illustrative description of the effect of sulfur content on solidification rate R, a schematic showing the angle theta is plotted in figure 6. Evidently, θ_1 is larger than θ_2, and consequently $\cos\theta_1$ is smaller than $\cos\theta_2$, implying that solidification rate R for Sul-1 is smaller than that for Sul-2. Without the consideration of the change in temperature gradient G, the hypothesis that the cooling rate GR increases while morphology parameter G/R drops with the increment of sulfur content can be drawn from simulation results. Consequently, the solidified grain is expected to be finer and equiaxed grain is prone to occurring in high-sulfur situations. Notably, it should be emphasized that the above hypothesis is obtained based on the assumption that temperature gradient G is constant for different sulfur levels. However, the sulfur-induced transition of melt pool dynamics will reasonably lead to the change of temperature gradient G, and the combined parametersGR

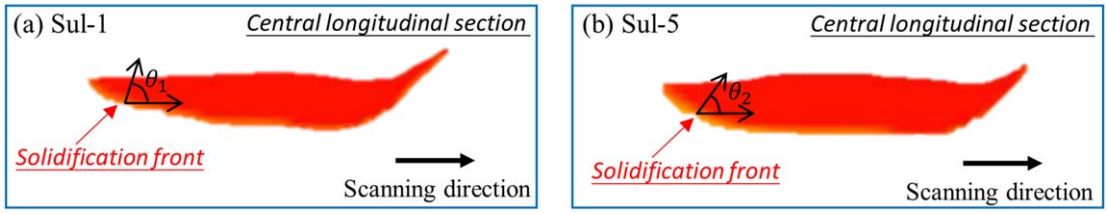


Figure 6. Schematics illustrating the solidification behavior of Sul-1 and Sul-5. (a) Sul-1, (b) Sul-5. (The reader is referred to the web version of this article for a better understanding).

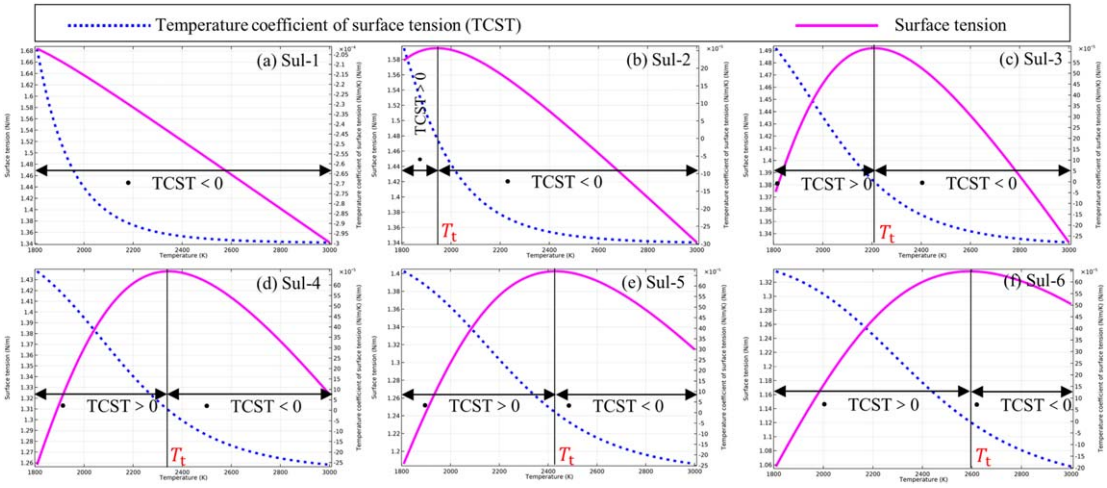


Figure 7. Plot of surface tension and temperature coefficient of surface tension (TCST) as the function of local temperature in Kelvin and sulfur content in percentage. (a) Sul-1, (b) Sul-2, (c) Sul-3, (d) Sul-4, (e) Sul-5, (f) Sul-6. (The reader is referred to the web version of this article for a better understanding).

and G/R depend on both the temperature gradient G and solidification velocity R. Thus, the real effect of sulfur-induced transitions on solidified grains is much more complex and worth being numerically and experimentally researched in depth in future work. Here, the impact of sulfur element on solidification behavior in LPBF is emphasized and a potential approach is provided to control the printing process for microstructure refinement and property improvement.

3.2. Thermo-capillarity transition

Figure 7(a) to (f) depict the variations of surface tension and temperature coefficient of surface tension (TCST) concerning local temperature and sulfur content for all six cases. Surface tension acts as the most influential driving force governing flow dynamics for laser-induced melt pool [26]. Notably, the sign transition of TCST can be induced when sulfur is contained in the printed powders. In the current simulation, the sulfur-induced effect on TCST is mathematically modelled, drawing from the description in reference [25]. As presented in figure 7, TCST is illustrated by the blue dotted line. The transition of TCST from positive to negative occurs between Sul-2 and Sul-6, with Sul-1, characterized by the extremely low sulfur concentration, maintaining a negative TCST throughout. Consequently, the surface tension, denoted by the pink solid line, steadily decreases in Sul-1. Conversely, a two-stage pattern in surface tension, comprising an initial increase followed by a decrease, divided by the transition temperature T_t (indicated by the black solid line), becomes evident as sulfur content increases from Sul-2 to Sul-6. T_t rises with increasing sulfur content, changing from 1942 K for Sul-2 to 2590 K for Sul-6, signifying that the sign transition of TCST is prone to occurring in low-sulfur situations, but the TCST transition disappears as sulfur concentration reaches extremely low levels (Sul-1). Thus, there exists a sulfur concentration threshold, distinguishing between Sul-1 and Sul-2, that determines the occurrence of TCST sign transition.

The direction of the flow pattern depends on the sign of TCST because surface tension is the dominant driving force in L-PBF [46]. As depicted in figure 8, three distinct flow patterns correspond to the three TCST types. The fluid flow within the melt pool of Sul-1 is anticipated to align with the flow pattern illustrated in

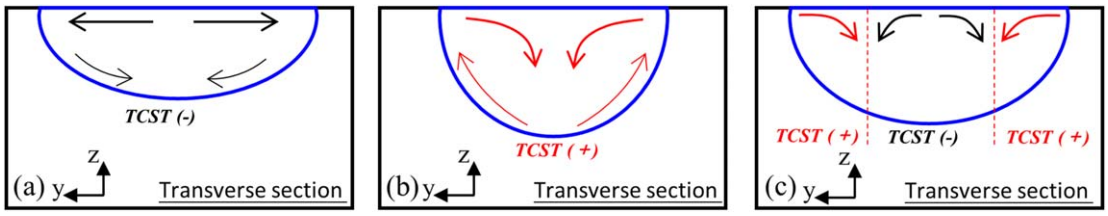


Figure 8. Flow patterns subject to distinct TCST signs. (a) TCST (-), (b) TCST(+), (c) Coexistence of TCST(-) and TCST(+). (The reader is referred to the web version of this article for a better understanding).

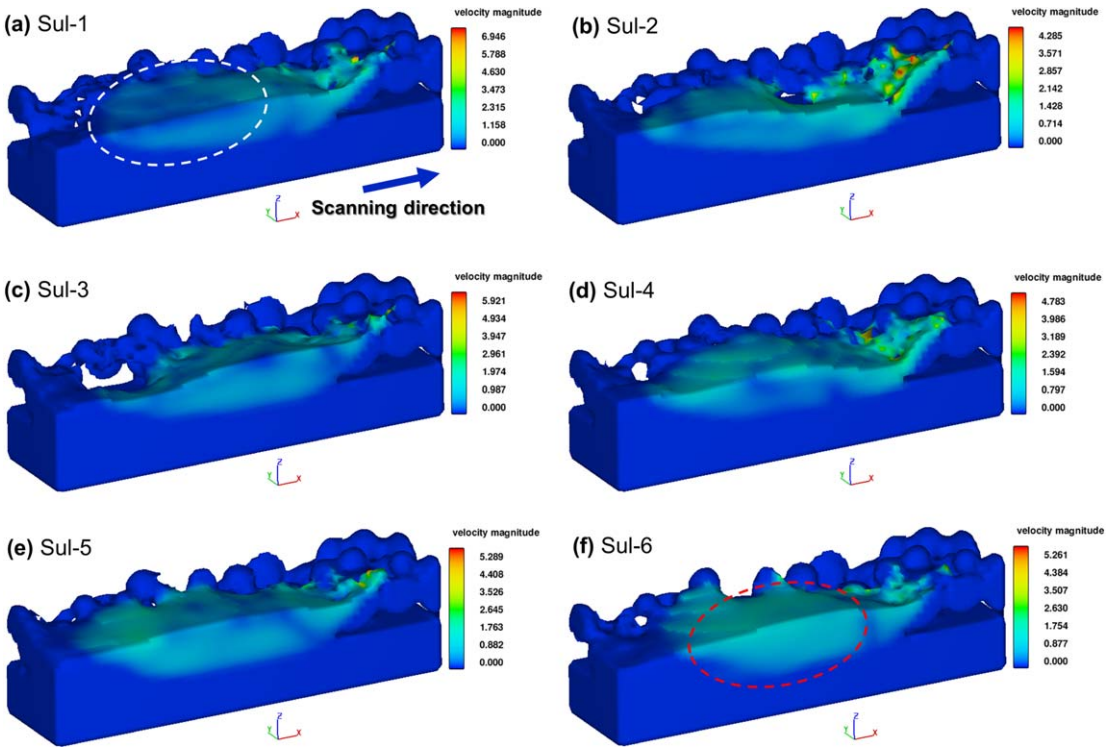


Figure 9. 3D velocity field for different cases. (a) Sul-1, (b) Sul-2, (c) Sul-3, (d) Sul-4, (e) Sul-5, (f) Sul-6. The color contour represents the magnitude of the velocity field (m/s) of the melt pool. (The reader is referred to the web version of this article for a better understanding).

figure 8(a) due to its consistently negative TCST, and a singular inward flow, as shown in figure 8(b), will be formed due to the continuously positive TCST. In cases where coexistence of TCST (-) and TCST (+) remain, a combined inward-outward flow is desired, as presented in figure 8(c).

3.3. Sulfur-effect on melt pool dynamics

The proposed 3D powder-scale model makes it possible to further discuss the impact of sulfur on melt pool dynamics, considering the variation in sulfur concentration. Figure 9 provides a depiction of the 3D velocity distribution across Sul-1 to Sul-6. As illustrated, the peak velocity occurs at front area and fluctuates around 5 m/s across these six scenarios. Sul-1 displays a noteworthy divergence in velocity distribution, characterized by a substantially higher velocity of 6.946 m/s. Conversely, as sulfur content increases, a more homogenous velocity distribution becomes evident in high-sulfur scenarios. For instance, in Sul-6, highlighted by the red dotted ellipse, the difference in velocity magnitude between the front and rear regions is relatively small. This contrasts with Sul-1, marked by the white dotted ellipse, where the velocity at the rear is less uniform.

To investigate the impact of sulfur on spatial and directional flow dynamics, fluid flow within the melt pool is analyzed by examining the flow dynamics in the longitudinal section, transverse section, and top view for all six scenarios. The spatial locations of the selected sections in the developed model are depicted in figure 10 for reference. In detail, the central section is chosen for the longitudinal view, while for the transverse section, the coordinate x = 0.55 mm is selected, with the laser starting at x = 0 mm. For the top

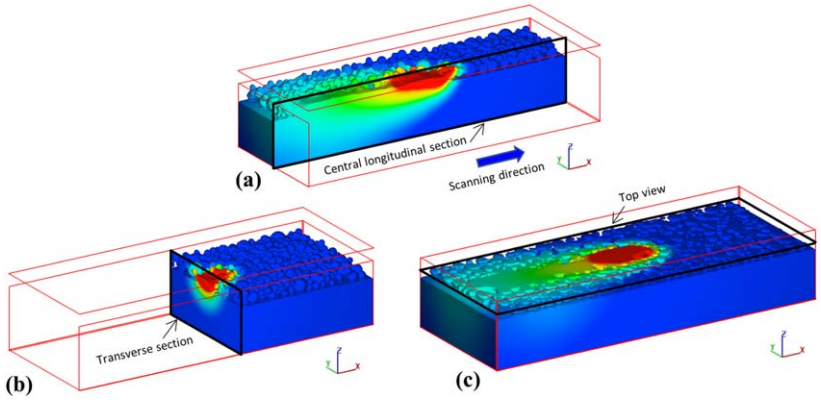


Figure 10. Spatial positions of the selected sections in the developed model. (a) Central longitudinal section, (b) Transverse section x = 0.55 mm, (c) Top view z = 0.1675 mm. Corresponding to the printing time of 1.1 ms when the melt pool is in the quasi-steady stage. (The reader is referred to the web version of this article for a better understanding).

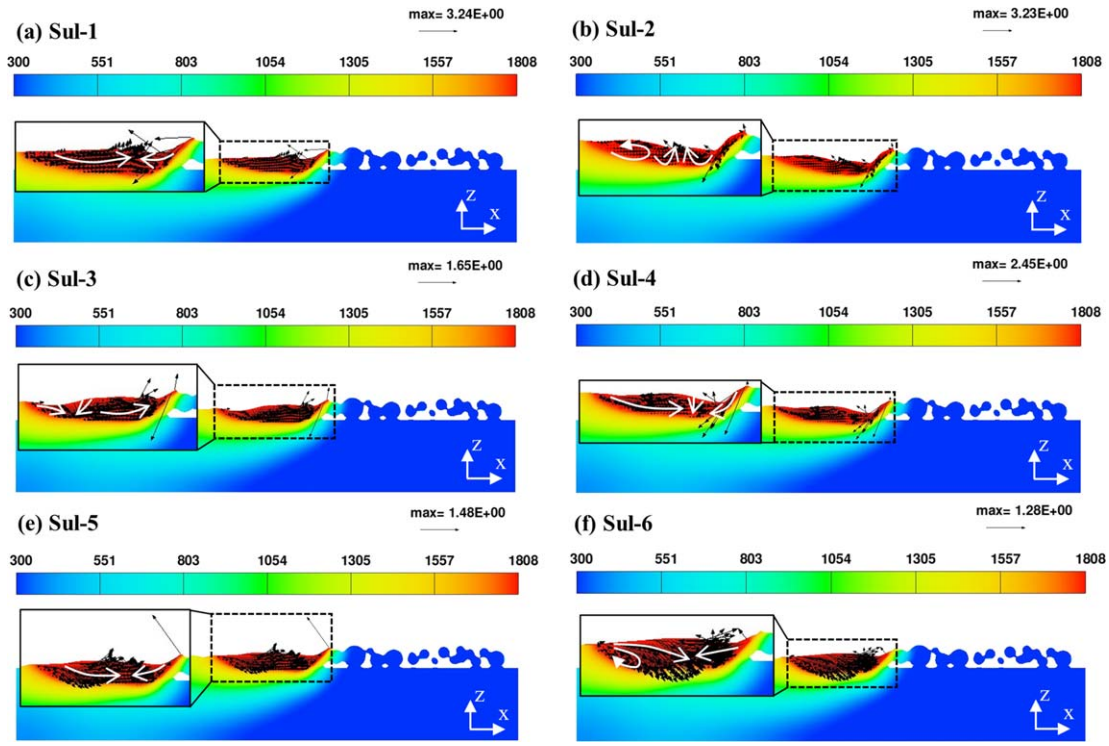


Figure 11. Spatial and directional flow characteristics at the central longitudinal section. (a) Sul-1, (b) Sul-2, (c) Sul-3, (d) Sul-4, (e) Sul-5, (f) Sul-6. The color contour represents the temperature field in Kelvin and the velocity field (m/s) is denoted by the black arrows. White arrows are used for the illustrations of the directions of branch flow and convection. (The reader is referred to the web version of this article for a better understanding).

view, the plane defined by z = 0.1675 mm is utilized, while the bottom surface of the powder bed is established at z = 0 mm.

As depicted in figure 11, branch flows are indicated by white arrows with hollow heads, while vortexes are highlighted by white arrows with solid heads. Along the longitudinal section, there is a noticeable decline in peak velocity, coupled with an increase in flow complexity as sulfur content rises. In Sul-1, only two distinct branch flows are observed, whereas in high-sulfur scenarios (except for Sul-5), the flow pattern involving three branch flow or two branch flow together with one additional vortex is found.

Of particular interest is the observation of vortexes with opposite directions in Sul-2 and Sul-6, characterized by anticlockwise and clockwise rotations, respectively. These vortexes are both situated at the melt pool tail, where transient temperatures are lower due to the Gaussian distribution of the laser source. Referring to figure 7, the transition temperature of TCST in Sul-2 is 1942 K, whereas in Sul-6, T_t is 2590 K. This suggests that the sign

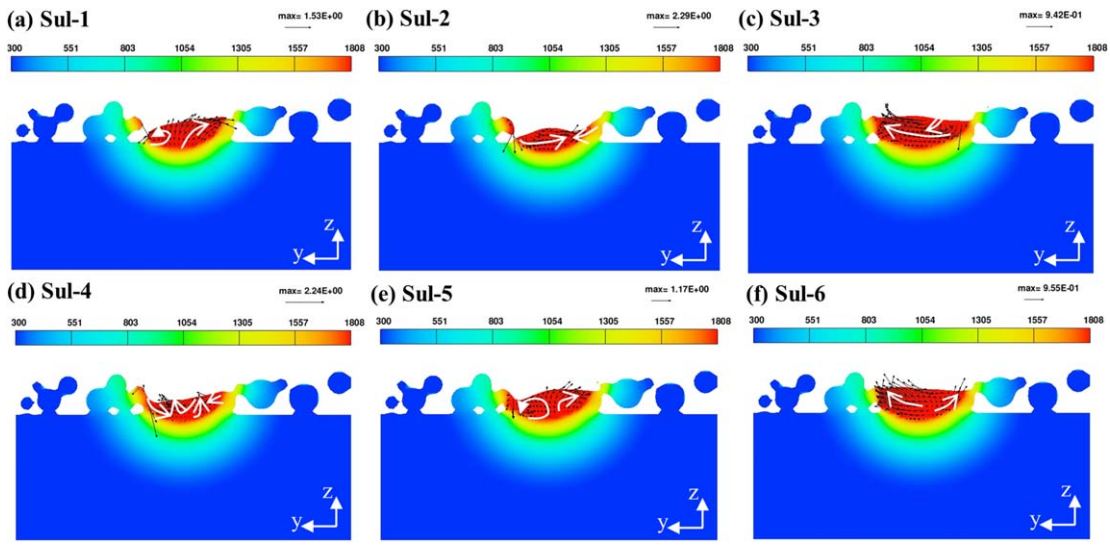


Figure 12. Spatial and directional flow characteristics at transverse section. (a) Sul-1, (b) Sul-2, (c) Sul-3, (d) Sul-4, (e) Sul-5, (f) Sul-6. The color contour represents the temperature field in Kelvin and the velocity field (m/s) is denoted by the black arrows. White arrows are used for the illustrations of the directions of branch flow and convection. (The reader is referred to the web version of this article for a better understanding).

transition of TCST from positive to negative is more likely to occur in the rear region with lower temperatures in Sul-2 rather than Sul-6. Consequently, TCST (−) at the rear portion in Sul-2 induces the flow pattern shown in figure 8(a): a bottom-up anticlockwise vortex. Conversely, TCST (+) at the tail region in Sul-6 results in the convection pattern illustrated in figure 8(b): a top-down clockwise vortex. These observations are well-supported by the simulated results for Sul-2 and Sul-6, as shown in figure 11(b) and figure 11(f), respectively. Furthermore, it's worth noting that both forward and backward flows are observed in all six scenarios. This bidirectional flow is considered advantageous for promoting the homogeneous mixing of molten powders and the melted substrate [46].

Flow characteristics at the transverse section are depicted in figure 12, positioned near the center of the laser heat source, which corresponds to the high-temperature region within the melt pool. It's worth noting that the sign transition of TCST from positive to negative tends to occur when local temperatures are significantly higher, as illustrated in figure 7. In figure 12, an anticlockwise vortex is observed in Sul-1 and Sul-5 due to TCST (−), while no clockwise vortex is observed in any of the six scenarios. Furthermore, the branch flow exhibits a bottom-up direction consistently across Sul-1 to Sul-6, corresponding to the flow pattern described for TCST (-) in figure 8(a).

Figure 13 presents the flow dynamics from a top view ($z = 0.1675$ mm). A notable observation is the presence of a blank area, representing a lack of liquid material in the melt pool. This blank area is prominent in Sul-1 through Sul-4 but is not as evident in Sul-5 and Sul-6. In high-sulfur situations, it is expected that more powders will be melted and fill this blank area. Additionally, all the vortexes observed from the top view exhibit clockwise rotation. They are positioned at the tail region in Sul-1 and Sul-3, and at the head part in Sul-5 and Sul-6. The peak velocity at the top view exhibits fluctuations from Sul-1 to Sul-6, but an overall decreasing trend is still discernible, which is 4.76 m/s for Sul-1 but drops to 1.29 m/s for Sul-6. A combined frontward and backward branch flow is observed from Sul-1 to Sul-5 but is absent in Sul-6. This discrepancy can be attributed to the significantly larger melt pool depth observed in Sul-6 from the simulated longitudinal sections in figure 11. Consequently, the flow characteristics in figure 13 (f) primarily reflect the dynamics at the upper region of the melt pool, resulting in the formation of a main single branch flow at the selected section. Moreover, it's worth noting that fluid flow near the melt pool bottom for Sul-6 is likely to exhibit increased complexity.

4. Conclusion

A 3D powder-scale transient computational fluid dynamics model is proposed to analyze the sulfur-induced transitions of thermo-capillary and melt pool dynamics. The current study focuses on the impact of sulfur content present in 316L powders and equivalent materials used worldwide. Some fundamental conclusions can be summarized as follows.

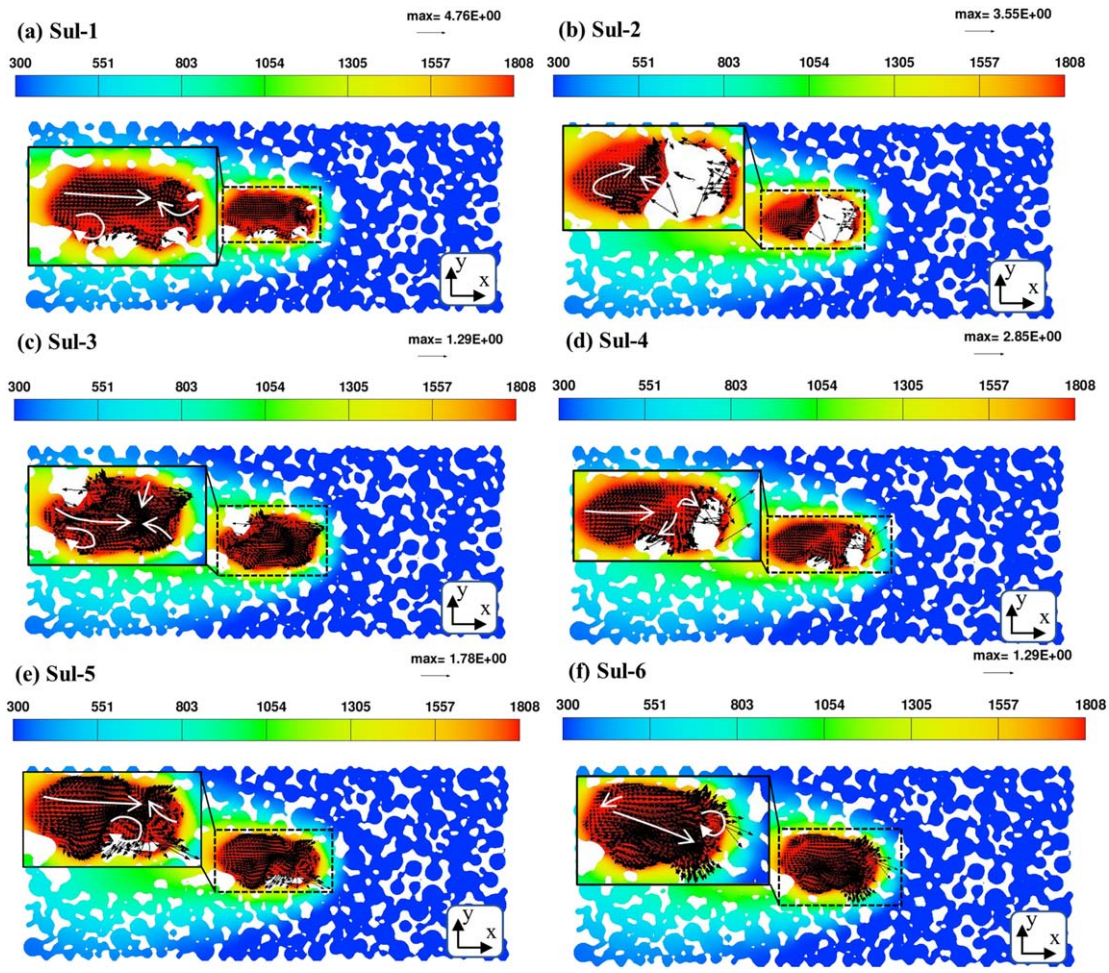


Figure 13. Spatial and directional flow characteristics at the top view section. (a) Sul-1, (b) Sul-2, (c) Sul-3, (d) Sul-4, (e) Sul-5, (f) Sul-6. The color contour represents the temperature field in Kelvin and the velocity field (m/s) is denoted by the black arrows. White arrows are used for the illustrations of the directions of branch flow and convection. (The reader is referred to the web version of this article for a better understanding).

(1) As sulfur content increases, the peak temperature within melt pool initially rises, subsequently decreases, resulting in a substantial reduction in track surface fluctuations. The solid/liquid interface transforms from a curved shape in low-sulfur situations to near flat in high-sulfur situations. This transition is expected to result in the occurrences of finer solidified grains and equiaxed grains.

(2) The sign transition of TCST is more likely to occur in low-sulfur situations and the transition temperature increases from 1942 K for Sul-2 (0.001%) to 2590 K for Sul-6 (0.03%). However, it disappears when sulfur concentrations reach extremely low levels (Sul-1, 0.0001%).

(3) A more uniform velocity distribution with the decreasing of velocity magnitude is presented in high-sulfur situations. Additionally, flow complexity, characterized by a greater presence of branch flows and vortexes, is significantly elevated as sulfur content increases.

(4) In the longitudinal section, TCST (−) induces a bottom-up anticlockwise vortex at the rear in low-sulfur situations, while TCST (+) results in a top-down clockwise vortex at the tail in high-sulfur situations. In the transverse section, bottom-up branch flows are observed across the sulfur content range. For the top view, the blank area observed in low-sulfur scenarios disappears with increasing sulfur content.

Acknowledgments

Zhiyong Li acknowledges the support from the National Natural Science Foundation of China (No. 12202448), and New Wire Additive Manufacturing (NEWAM) United Kingdom program (EP/R027218/1) granted by

Engineering and Physical Sciences Research Council. Xinfeng Kan is grateful for the financial help from Jiangsu University (High-tech ship) Collaborative Innovation Center (1174872301-7).

Data availability statement

All data that support the findings of this study are included within the article (and any supplementary files).

ORCID iDs

Zhiyong Li https://orcid.org/0000-0003-3106-4333
Xinfeng Kan https://orcid.org/0000-0002-9986-6271

References

[1] Debroy T, Wei H L, Zuback J S, Mukherjee T, Elmer J W, Milewski J O, Beese A M, Wilson-Heid A, De A and Zhang W 2018 Additive manufacturing of metallic components–process, structure and properties *Prog. Mater Sci.* **92** 112–224
[2] Gu D D, Shi X Y, Poprawe R, Bourell D L, Setchi R and Zhu J H 2021 Material-structure-performance integrated laser-metal additive manufacturing *Science* **372** eabg1487
[3] Zhang D, Qiu D, Gibson M A, Zheng Y, Fraser H L, StJohn D H and Easton M A 2019 Additive manufacturing of ultrafine-grained high-strength titanium alloys *Nature* **576** 91–5
[4] Yuan Y, Zhang Y F, Qiao Y, Xie J, Xu Q F, Qi Y S, Zhang W F and Chen P W 2023 Effect of build orientation on dynamic compressive behaviour of Ti-6Al-4V alloy fabricated by selective laser melting *Materials Science and Engineering:* A **862** 144440
[5] Poudel A, Yasin M S, Ye J, Liu J, Vinel A, Shao S and Shamsaeit. N 2022 Feature-based volumetric defect classification in metal additive manufacturing *Nat. Commun.* **13** 6369
[6] Hazarika Mallikarjuna B, Krishna P, Balla V K and Bontha S 2016 Numerical modelling of laser additive manufacturing processes *NAFEMS India Regional Conference, Bangalore*
[7] Mallikarjuna B, Bontha S, Krishna P and Balla V K 2021 Characterization and thermal analysis of laser metal deposited γ-TiAl thin walls *Journal of Materials Research and Technology* **15** 6231–43
[8] Kan X F, Yin Y J, Yang D C, Li W and Sun J Q 2021 Micro pool characteristics of 316L and the influence of sulfur during SLM *Opt. Laser Technol.* **142** 107136
[9] Sanchez S, Smith P, Xu Z, Gaspard G, Hyde C J, Wits W W, Ashcroft I A, Chen H and Clare A T 2021 Powder bed fusion of nickel-based superalloys: a review *Int. J. Mach. Tools Manuf.* **165** 103729
[10] Bidare P, Bitharas I, Ward R M, Attallah M M and Moore A J 2018 Fluid and particle dynamics in laser powder bed fusion *Acta Mater.* **142** 107–20
[11] Li E, Zhou Z Y, Wang L, Zou R P and Yu A B 2022 Numerical studies of melt pool and gas bubble dynamics in laser powder bed fusion process *Additive Manufacturing* **56** 102913
[12] Guo Q L, Zhao C, Escano L I, Young Z, Xiong Lh, Fezzaa K, Everhart W, Brown B, Sun T and Chen L Y 2018 Transient dynamics of powder spattering in laser powder bed fusion additive manufacturing process revealed by *in situ* high-speed high-energy x-ray imaging *Acta Mater.* **151** 169–80
[13] Gunenthiram V, Peyre P, Schneider M, Dal M, Coste F, Koutiri I and Fabbro R 2018 Experimental analysis of spatter generation and melt-pool behavior during the powder bed laser beam melting process *J. Mater. Process. Technol.* **251** 376–86
[14] Spears T G and Gold S A 2016 In-process sensing in selective laser melting (SLM) additive manufacturing *Integrating Materials and Manufacturing Innovation* **5** 16–40
[15] Krauss H, Zeugner T and Zaeh M F 2014 Layerwise monitoring of the selective laser melting process by thermography *Phys. Proc.* **56** 64–71
[16] Ly S, Rubenchik A M, Khairallah S A, Guss G and Matthews M J 2017 Metal vapor micro-jet controls material redistribution in laser powder bed fusion additive manufacturing *Sci. Rep.* **7** 4085
[17] Masmoudi A, Bolot R and Coddet C 2015 Investigation of the laser-powder-atmosphere interaction zone during the selective laser melting process *J. Mater. Process. Technol.* **225** 122–32
[18] Ye W, Zhang S, Mendez L L, Farias M, Li J, Xu B, Li P and Zhang Y 2021 Numerical simulation of the melting and alloying processes of elemental titanium and boron powders using selective laser alloying *J. Manuf. Processes* **64** 1235–47
[19] Mukherjee T, Wei H L, De A and Debroy T 2018 Heat and fluid flow in additive manufacturing–Part II: Powder bed fusion of stainless steel, and titanium, nickel and aluminum base alloys *Comput. Mater. Sci.* **150** 369–80
[20] Vastola G, Pei Q X and Zhang Y W 2018 Predictive model for porosity in powder-bed fusion additive manufacturing at high beam energy regime *Additive Manufacturing* **22** 817–22
[21] Ge W J, Han S, Na S J and Fuh J Y H 2021 Numerical modelling of surface morphology in selective laser melting *Comput. Mater. Sci.* **186** 110062
[22] Wang Z and Liu M 2020 Semi-resolved CFD–DEM for thermal particulate flows with applications to fluidized beds *Int. J. Heat Mass Transfer* **159** 120150
[23] Wang Z, Teng Y and Liu M 2019 A semi-resolved CFD–DEM approach for particulate flows with kernel based approximation and Hilbert curve based searching strategy *J. Comput. Phys.* **384** 151–69
[24] Wang Z and Liu M 2019 Dimensionless analysis on selective laser melting to predict porosity and track morphology *J. Mater. Process. Technol.* **273** 116238
[25] Sahoo P, Debroy T and McNallan M J 1988 Surface tension of binary metal—surface active solute systems under conditions relevant to welding metallurgy *Metall. Mater. Trans.*B **19** 483–91
[26] Li Z Y, Yu G, He X L, Li S X, Tian C X and Dong B X 2020 Analysis of surface tension driven flow and solidification behavior in laser linear welding of stainless steel *Opt. Laser Technol.* **123** 105914
[27] Wei H L, Pal S, Manvatkar V, Lienert T J and DebRoy T 2015 Asymmetry in steel welds with dissimilar amounts of sulfur *Scr. Mater.* **108** 88–91

[28] Shen H, Pan Y Q, Zhou J and Yao Z Q 2017 Forming mechanism of bump shape in pulsed laser melting of stainless steel *J. Heat Trans-T ASME* **139** 062301
[29] Gan Z T, Yu G, He X L and Li S X 2017 Surface-active element transport and its effect on liquid metal flow in laser assisted additive manufacturing *Int. Commun. Heat Mass Transfer* **86** 206–14
[30] Heiple C R, Roper J R and Stagner R T 1983 Surface active element effects on the shape of GTA, laser, and electron beam welds *Welding Research Supplement* **62** 772-s
[31] Pitscheneder W, Debroy T, Mundra K and Ebner R 1996 Role of sulfur and processing variables on the temporal evolution of weld pool geometry during multikilowatt laser beam welding of steels *Welding Research Supplement* **75** 71–80
[32] Zhao Y, Lei Y and Shi Y 2005 Effects of surface-active elements sulfur on flow patterns of welding pool *Journal of Materials Sciences and Technology* **21** 408–14
[33] Kidess A, Kenjereš S and Kleijn C R 2016 The influence of surfactants on thermocapillary flow instabilities in low prandtl melting pools *Phys. Fluids* **28** 06216
[34] Ebrahimi A, Kleijn C R and Richardson I M 2019 The influence of surface deformation on thermocapillary flow instabilities in low Prandtl melting pools with surfactants *Proceedings of the 5th World Congress on Mechanical, Chemical, and Material Engineering, MCM* 2019, Lisbon, Portugal
[35] Ebrahimi A, Kleijn C R and Richardson I M 2021 A simulation-based approach to characterise melt-pool oscillations during gas tungsten arc welding *Int. J. Heat Mass Transfer* **164** 120535
[36] Ebrahimi A, Kleijn C R, Hermans M J M and Richardson I M 2021 The effects of process parameters on melt-pool oscillatory behaviour in gas tungsten arc welding *J. Phys. D: Appl. Phys.* **54** 275303
[37] Le T N and Lo Y L 2019 Effects of sulfur concentration and marangoni convection on melt-pool formation in transition mode of selective laser melting process *Mater. Des.* **179** 107866
[38] Aucott L *et al* 2018 Revealing internal flow behaviour in arc welding and additive manufacturing of metals *Nat. Commun.* **9** 5414
[39] Yan W T, Ge W J, Qian Y, Lin S, Zhou B, Liu W K, Lin F and Wagner G J 2017 Multi-physics modeling of single/multiple-track defect mechanisms in electron beam selective melting *Acta Mater.* **134** 324–33
[40] Courtois M, Carin M, Le Masson P, Gaied S and Balabane M 2016 Guidelines in the experimental validation of a 3D heat and fluid flow model of keyhole laser welding *J. Phys. D: Appl. Phys.* **49** 155503
[41] Mu Z Y, Chen X, Zheng Z C, Huang A G and Pang S Y 2019 Laser cooling arc plasma effect in laser-arc hybrid welding of 316L stainless steel *Int. J. Heat Mass Transfer* **132** 861–70
[42] Simonds B J, Tanner J, Artusio-Glimpse A B, Williams P, Parab N D, Zhao C and Sun T 2021 The causal relationship between melt pool geometry and energy absorption measured in real time during laser-based manufacturing *Applied Materials Today* **23** 101049
[43] Ebrahimi A, Sattari M, Bremer S J L, Luckabauer M, Römer G R B E, Richardson I M, Kleijn C R and Hermans M J M 2022 The influence of laser characteristics on internal flow behaviour in laser melting of metallic substrates *Mater. Des.* **214** 110385
[44] Voller V and Prakash C 1987 A fixed grid numerical modelling methodology for convection–diffusion mushy region phase-change problems *Int. J. Heat Mass Transfer* **30** 1709–19
[45] Ebrahimi A, Kleijn C R and Richardson I M 2019 Sensitivity of numerical predictions to the permeability coefficient in simulations of melting and solidification using the enthalpy-porosity method *Energies.* **12** 4360
[46] Li Z, He X, Li S, Kan X, Yin Y and Yu G 2023 Sulfur-induced transitions of thermal behavior and flow dynamics in laser powder bed fusion of 316L powders *Thermal Science and Engineering Progress* **45** 102072
[47] Li Z Y, Yu G, He X L, Li S X and Li Z X 2020 Fluid flow and solute dilution in laser linear butt joining of 304SS and Ni *Int. J. Heat Mass Transfer* **161** 120233
[48] Kou S 2003 *Welding Metallurgy* (Hoboken, NJ: Wiley)
[49] Yan W T 2017 *Multi-scale Multi-physics Modeling of Electron Beam Selective Melting Process* Tsinghua University, Thesis for PhD



https://dspace.org/

Impact of sulfur content on thermo-capillarity and melt pool dynamics in laser powder bed fusion of 316L powders

Li, Zhiyong; Kan, Xinfeng; Yin, Yanjun

2023-12-05
IOP Publishing
https://doi.org/10.1088/2053-1591/ad0dd0
Li Z, Kan X, Yin Y. (2023) Impact of sulfur content on thermo-capillarity and melt pool dynamics in laser powder bed fusion of 316L powders. Materials Research Express, Volume 10, Issue 12, December 2023, Article number 126502

Downloaded from a DSpace repository. https://dspace.org/